ELSEVIER

Journal of Fluids and Structures 25 (2009) 831–847

JOURNAL OF FLUIDS AND STRUCTURES

www.elsevier.com/locate/jfs

Direct numerical simulation of three-dimensional flow past a yawed circular cylinder of infinite length

Ming Zhao*, Liang Cheng, Tongming Zhou

School of Civil and Resource Engineering, The University of Western Australia, 35 Stirling Highway, Crawley, WA 6009, Australia

Received 7 March 2008; accepted 1 March 2009
Available online 5 May 2009

Abstract

Direct numerical simulation of flow past a stationary circular cylinder at yaw angles (α) in the range of 0–60° was conducted at Reynolds number of 1000. The three-dimensional (3-D) Navier–Stokes equations were solved using the Petrov–Galerkin finite element method. The transition of the flow from 2-D to 3-D was studied. The phenomena that were observed in flow visualization, such as the streamwise vortices, the vortex dislocation and the instability of the shear layer, were reproduced numerically. The effects of the yaw angle on wake structures, vortex shedding frequency and hydrodynamic forces of the cylinder were investigated. It was found that the Strouhal number at different yaw angles (α) follows the independence principle. The mean drag coefficient agrees well with the independence principle. It slightly increases with the increase of α and reaches a maximum value at $\alpha = 60°$, which is about 10% larger than that when $\alpha = 0°$. The root-mean-square (r.m.s.) values of the lift coefficient are noticeably dependent on α.

Keywords: Direct numerical simulation; Circular cylinder; Three-dimensional; Vortex shedding

1. Introduction

When a cylinder is exposed to a steady approaching flow, the wake structure downstream of the cylinder is three-dimensional (3-D) as long as the Reynolds number (Re) is larger than about 170, even before it becomes turbulent (Roshko, 1954; Bloor, 1964; Williamson, 1988; Norberg, 2001). The Reynolds number is defined by $\mathrm{Re} = UD/v$, where U is the incoming velocity in the streamwise direction, D is the cylinder diameter, v is the fluid kinematic viscosity. The wake flow is in the transitional regime when Reynolds number is between 170 and 300 and becomes fully turbulent as Reynolds number is larger than about 400. In most of civil and mechanical engineering applications, the Reynolds number is usually much larger than 400. Therefore, the wake flow is normally turbulent.

Extensive studies on turbulent wake flows past a circular cylinder have been conducted using both experimental and numerical methods. Williamson (1988, 1991, 1992) investigated the three-dimensional transition of the flow behind a circular cylinder. It was found that the three-dimensionality and turbulence in a wake are triggered by instabilities within the vortex formation region. The instabilities include the generation of the small-scale streamwise vortices, large-scale vortex dislocations and small-scale shear-layer instability vortices. When Reynolds number is in the turbulent regime, the hydrodynamic forces on the circular cylinder fluctuate with time due to the vortex shedding. Schewe (1983)

*Corresponding author. Tel.: +61 864887356; fax: +61 864881044.
E-mail address: zhao@civil.uwa.edu.au (M. Zhao).

0889-9746/$ - see front matter © 2009 Elsevier Ltd. All rights reserved.
doi:10.1016/j.jfluidstructs.2009.02.004

reported the experimental results of the drag coefficient C_D and lift coefficient C_L over a wide range of Reynolds number. The C_D and C_L are defined by $C_D = F_D/(\rho DU^2/2)$ and $C_L = F_L/(\rho DU^2/2)$, where ρ is the fluid density, F_D and F_L are drag and lift forces on a unit length of a cylinder in the flow direction and that in the cross-flow direction, respectively. According to Schewe's results, the force coefficients and the vortex shedding frequency are not sensitive to Reynolds number as long as the latter is in the subcritical regime ($300 < \mathrm{Re} < 3 \times 10^5$).

Since the wake flow behind a circular cylinder is three-dimensional, it is desirable that the flow is simulated by a 3-D model in order to obtain a full understanding of the wake flow. Two-dimensional numerical models tend to overestimate the lift coefficient and the vortex shedding frequency because the variation of flow in the cylinder's spanwise direction (Kang, 2006; Zhao et al., 2007; Tsutsui et al., 1997) is ignored. Karniadakis and Triantafyllou (1992) and Zhang and Dalton (1998) simulated the 3-D flow past a circular cylinder using three-dimensional models for Reynolds number in the range of 100–500. Their findings about the transition of the flow to turbulence agree well with those found in experiments (Williamson, 1992). Lei et al. (2001) studied the effect of the computational domain size on the accuracy in the simulation of 3-D flow past a circular cylinder. They found that the size of the computational domain in the spanwise direction must be at least four times the cylinder diameter in order to simulate the 3-D wake flow accurately.

In many engineering applications, such as the flow past cables, subsea pipelines, risers, etc., the direction of the flow may not be perpendicular to the structure. This kind of flows can be represented by a wake flow downstream of a yawed cylinder in laboratory studies and numerical simulations. In this case, the fluid velocity in the spanwise as well as in the cross-flow directions may be of similar magnitudes. It is expected that the three-dimensional effect and the wake flow patterns of a yawed cylinder will be stronger than that of a wake when the cylinder is perpendicular to the flow. Flows past a yawed cylinder have been studied by a number of investigators both experimentally [e.g. King (1977); Ramberg (1983); Kozakiewicz et al. (1995); Thakur et al. (2004)] and numerically [e.g. Chiba and Horikawa (1987); Marshall (2003); Lucor and Karniadakis (2003)]. Experimental results showed that the force coefficients and the Strouhal number, which are normalized by the velocity component perpendicular to the cylinder, are approximately independent on the yaw angle. This is often called the independence principle or the cosine law in the literature. Kozakiewicz et al. (1995) found that the independence principle can be applied to stationary cylinders in the vicinity of a plane wall for a yawed angle between 0° and 45°. In case of flow past a yawed cylinder of finite length, it was shown that the wake vortices far from the upstream end of the cylinder are approximately parallel to the cylinder. The vortices near the upstream end of the cylinder are aligned at an angle larger than the cylinder yaw angle (Ramberg, 1983; Thakur et al., 2004). Lucor and Karniadakis (2003) simulated flow past a yawed cylinder of infinite length at two large yaw angles, namely 60° and 70°. They reported that the vortex shedding angles of the vortices in the wake of a yawed cylinder are somewhat less than the cylinder's yaw angle.

In the present study, flow past an infinitely long stationary circular cylinder at yawed angles in the range of 0–60° was investigated numerically. The definition of the coordinate system and the yaw angle α are given in Fig. 1, where $\alpha = 0°$ represents the right attack angle case (i.e. the flow direction is perpendicular to the cylinder). Direct simulation of the Navier–Stokes equations was performed without employing any turbulent models. The Reynolds number Re was 1000. This Reynolds number was selected based on following considerations. Firstly, the wake flow at this Reynolds number is fully turbulent according to previous studies. It has been shown that the hydrodynamic forces are not sensitive to the Reynolds number as long as the later is in the subcritical regime ($300 < \mathrm{Re} < 3 \times 10^5$). Secondly a relative small value of Reynolds number in the subcritical regime allows a direct simulation of the Navier–Stokes equations being carried out with affordable computational costs. Therefore, the present choice of the Reynolds number was a compromise of the flow regimes and the computational cost. The effects of the yaw angles on the wake flow, the hydrodynamic force and the vortex shedding frequency were examined.

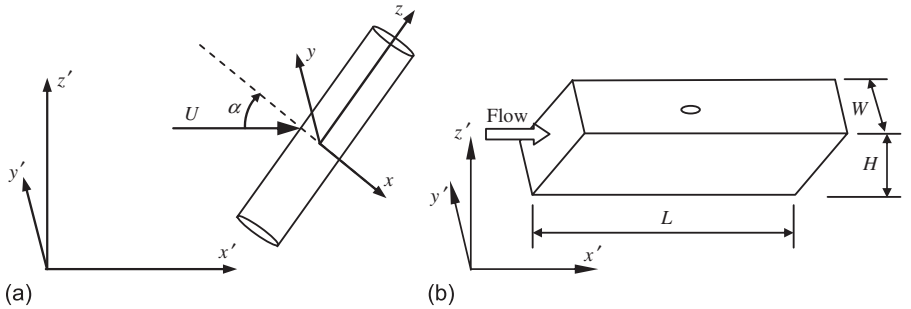

Fig. 1. Definition of the coordinate system and the computational domain: (a) coordinate system and (b) computational domain.

2. Numerical method

2.1. Governing equations and boundary conditions

The nondimensional Navier–Stokes equations and the continuity equation in Cartesian coordinate system $x'y'z'$ (Fig. 1) are

$$u_{i,t} + u_j u_{i,j} + p_{,i} - \frac{1}{\mathrm{Re}} u_{i,jj} = 0, \tag{1}$$

$$u_{i,i} = 0, \tag{2}$$

where u_i is the velocity component in the x_i-direction, $(x_1,x_2,x_3) = (x',y',z')$, the subscripts in $f_{,t}$ and $f_{,i}$ represent the derivatives of f with respect to time t and x'_i, respectively, and p is the pressure. The computational domain is shown in Fig. 1(b). In the present study, flow past a cylinder of infinite length was simulated by a truncated domain and a periodic boundary condition at the top and bottom boundaries. The left and right boundaries are parallel to the cylinder axis. The initial values of the velocity and the pressure in the whole domain are zero. In order to see how the vortex shedding is developed, no perturbation is introduced. The boundary conditions for the governing equations are as follows:

At the left boundary (inlet), a unit velocity component in the x'-direction is given and the velocity components in the y' and z' directions are zero. The pressure gradient in the flow direction is zero. At the right boundary the pressure and the velocity gradients in the x'-direction are zero. At the two-side boundaries that are parallel to the x'–z' plane, a free-slip boundary condition is employed, namely, the velocity component and the pressure gradient perpendicular to the boundary are zero.

When the flow approaches the cylinder at a yawed angle, the velocity in the cylinder's spanwise direction can be significant. The free-slip boundary condition is not a good choice at the top and bottom boundaries (two boundaries that are parallel to the x'–y' plane) because it prohibits the flow to pass these boundaries. In this study, a periodic condition was imposed by setting velocity and pressure values at the top and the bottom boundaries to be equal to each other. At the cylinder surface the no-slip boundary condition is applied. The Navier–Stokes equations were solved using the Petrov–Galerkin finite element method (PG-FEM). Details of the PG-FEM can be found in Appendix.

3. Numerical results

Numerical simulations were carried out at Reynolds number $\mathrm{Re} = 1000$ and yaw angles ranging from 0° to 60°. The cases for $\alpha > 60^\circ$ were not covered in this study because of the difficulties in generating quality computational meshes. It is expected that the dimensional force in the cross cylinder direction for $\alpha > 60^\circ$ is much smaller than in other cases. So, flows with $\alpha > 60^\circ$ may not be of as much engineering interests as those with smaller yaw angles. Parallel computational program code is developed for the calculations conducted in this study. The calculations were performed on a cluster of computers located in the advanced computing facility in Western Australia (iVEC). Thirty-two processors are used for each of the calculations. The simulations were carried out up to the non-dimensional time of $Ut/D = 450$ to ensure that vortex shedding is fully developed.

3.1. Mesh dependence study

A mesh dependence study was carried out before the effect of α on the flow was investigated. Three kinds of meshes were used to simulate the flow for $\alpha = 0^\circ$, i.e. coarse, medium and fine meshes. The length of the cylinder (L_s) is $9.6D$. Table 1 shows the mesh characteristics, the mean drag coefficient, r.m.s. lift coefficient and the Strouhal number computed according to the three kinds of meshes. In the present study, the drag and lift coefficients are defined as

$$C_D = F_D/(\rho D L_s U_n^2/2), \quad C_L = F_L/(\rho D L_s U_n^2/2), \tag{3a, b}$$

where F_D is the drag force in the x-direction, F_L is the lift force in the y-direction, L_s is the cylinder length, $U_n (\equiv U\cos\alpha)$ is the velocity component normal to the cylinder and U is the incoming velocity. The coordinates x and y are shown in Fig. 1. The F_D and F_L are calculated by integrating the pressure and the shear stress along the whole cylinder surface. The Strouhal number is defined by $\mathrm{St} = f_s D/U_n$ with f_s being the frequency of the fluctuating lift force.

The mean drag coefficient $\bar{C}_D$ for the fine mesh is 1.17, which is in the range of the measured results between 1.0 and 1.2 (Braza et al., 1986; Niemann and Hölscher, 1990). The Strouhal number for the fine mesh is 0.21, which agrees well

Table 1
Mesh dependence check for $\alpha = 0^\circ$ and Re = 1000.

Mesh density	Coarse	Medium	Fine
Node number	286 000	426 800	743 461
Node number along cylinder circumstance	80	80	96
Node number along cylinder length	64	96	96
Mesh size Δ_1 next to the cylinder surface	0.0025	0.0015	0.001
Mean drag coefficient $\bar{C}_D$	1.092	1.141	1.170
R.m.s. lift coefficient C'_L	0.310	0.327	0.335
Strouhal number (St)	0.202	0.209	0.210

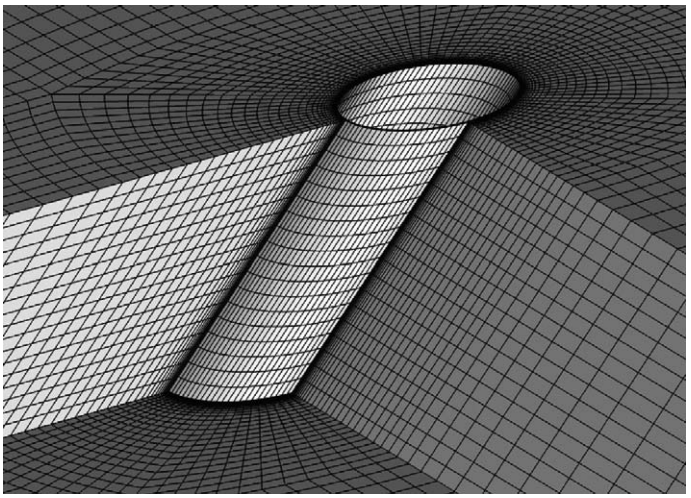

Fig. 2. Computational mesh for $\alpha = 45^\circ$.

with the experimental data between 0.207 and 0.22 (Roshko, 1954). By comparing the results for the mean drag coefficient, r.m.s. lift coefficient and Strouhal number calculated using the medium mesh and those using the fine mesh, it can be seen that the differences of the above quantities between the two meshes are 2.5%, 2.4% and 0.5%, respectively. Therefore, the meshes used for yaw angles examined were of densities the same as that of the fine mesh described in Table 1.

It has been shown that the computational domain size in the cylinder spanwise direction must be larger than $4D$ in order to simulate the three-dimensional wake flow accurately (Lei et al., 2001). In this study, the computational domain size in the z'-direction (Fig. 1) was kept at $9.6D$ for all values of α, which resulted in the cylinder length varying with α as $L_s = 9.6/\cos\alpha$ (Fig. 1). The width (W) and the length (L) of the domain were $20D$ and $45D$, respectively. The distance between the cylinder and the inlet boundary was $16D$. Fig. 2 shows the computational mesh around the cylinder for yaw angle $\alpha = 45^\circ$. The element size in the cylinder spanwise direction was $0.1D$. The node number along the circumference of a cross section of the cylinder surface was 96. The near wall mesh density can be evaluated by the nondimensional distance of a nodal point to the wall: $y^+ = u_f \Delta/\nu$, where Δ is the distance from the wall and u_f is the friction velocity. The nondimensional distance of the nodes next to the wall was less than 0.3 for all values of α and at least three layers of grid points were located within $y^+ < 1$. The number of nodal points increases with the increase of α. It was 743,461 for $\alpha = 0^\circ$ and 1,479,561 for $\alpha = 60^\circ$.

3.2. Wake flow features

Fig. 3 shows the time history of the total and the sectional force coefficients for $\alpha = 0^\circ$. The total force coefficients are defined by Eq. 3(a) and (b) while the sectional force coefficients are defined by

$$C_D(z) = F_D(z)/(\rho D U_n^2/2), \quad C_L(z) = F_L(z)/(\rho D U_n^2/2), \tag{4a, b}$$

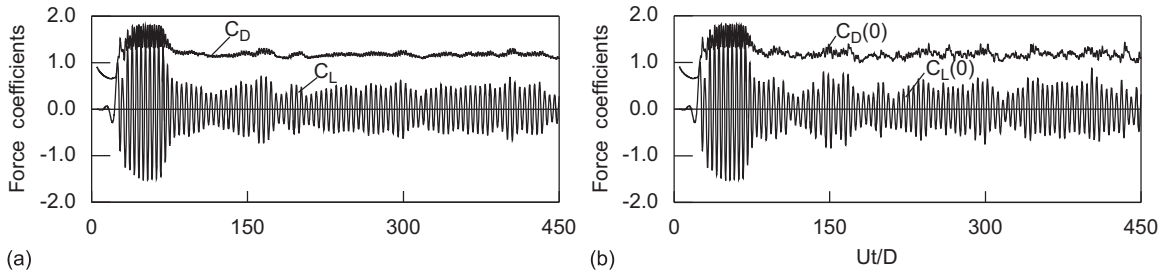

Fig. 3. Time history of force coefficients for $\alpha = 0^\circ$: (a) total force coefficients for $\alpha = 0^\circ$ and (b) sectional force coefficients for $\alpha = 0^\circ$.

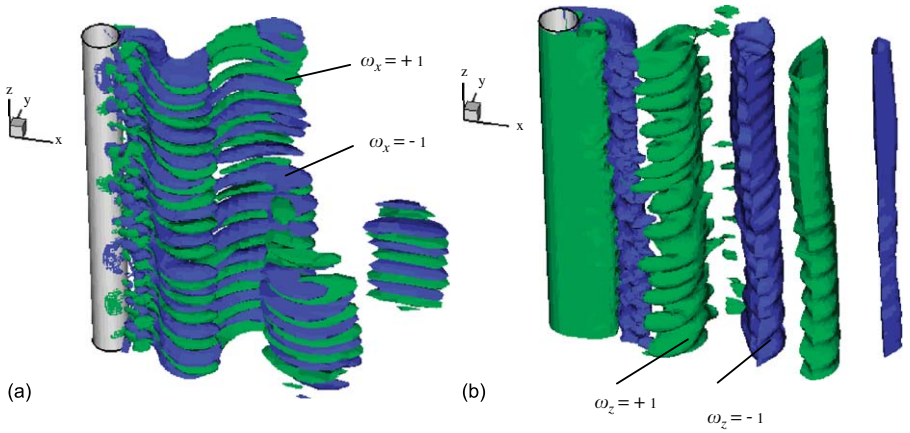

Fig. 4. Vorticity iso-surfaces for $\alpha = 0^\circ$ and $Ut/D = 75$: (a) $|\omega_x| = 1$ and (b) $|\omega_z| = 1$.

where $F_D(z)$ and $F_L(z)$ are the drag and lift forces acting on a unit length of the cylinder, respectively. They are obtained by integrating the pressure and shear stress over the circumference of a cross section of the cylinder surface.

The periodicity of the force fluctuations can be clearly seen in Fig. 3. Because the computational mesh, the boundary condition and the approaching flow are symmetric with respect to the x–z plane, the wake flow remains two-dimensional for a long time after the start of the computation. The flow is two-dimensional and the vortex shedding flow does not vary along the cylinder's spanwise direction until $Ut/D = 65$. The forces fluctuate at high amplitude and have a good repeatability when the flow is 2-D. The transition of the flow from 2-D to 3-D occurs at around $Ut/D = 65$. When the wake flow becomes totally three-dimensional ($Ut/D \geqslant 85$), the fluctuating amplitudes of the drag and lift decrease dramatically, and the amplitudes of the force coefficients vary with time. The total force coefficients C_D and C_L shown in Fig. 3(a) are actually the results of the averaged sectional force coefficients $C_D(z)$ and $C_L(z)$ over the total cylinder length. The averaging process filters out the variation of the forces along the cylinder axis. This is the reason why the curves of the total force coefficients (Fig. 3(a)) are smoother than those of the sectional force coefficients (Fig. 3(b)). In the numerical modelling, the time period required for transition of the wake flow from 2-D to 3-D can be shortened by introducing an artificial disturbance (for example, by introducing an uneven velocity distribution along the cylinder spanwise direction) at the early stage of the calculation. This would reduce the computational time consumption remarkably. The disturbance is not used here because the transition from 2-D to 3-D is one of the objectives of the present investigation.

The wake flow in the transitional period between $Ut/D = 65$ and 85 is quite similar to that at low Reynolds number in the transitional regime (Williamson, 1992). Fig. 4 shows the three-dimensional iso-surfaces of the streamwise and spanwise vorticity components behind the cylinder for $\alpha = 0^\circ$ at $Ut/D = 75$ when the wake flow transits from 2-D to 3-D. The vorticity components are defined as $\omega_x = \partial w/\partial y - \partial v/\partial z$, $\omega_y = \partial u/\partial z - \partial w/\partial x$ and $\omega_z = \partial v/\partial x - \partial u/\partial y$. Here u, v and w are the velocity components in the x, y and z directions, respectively. The green colour represents positive iso-surfaces and the blue colour represents negative ones in Fig. 4. At this stage, the streamwise vortices occur. The variation of the streamwise vortices in the spanwise direction is very regular. A row of rib-like streamwise vortices are generated and shed from the cylinder at nearly the same phase. The vortex shedding shown in Fig. 4(a) is quite similar

to the finer-scale streamwise vortex structure observed by Williamson (1992). Williamson (1992) reported that the spanwise wavelength is $3D$ for $\mathrm{Re}=180$ and $1D$ for $\mathrm{Re}=230$. The spanwise wavelength in Fig. 4 is about $0.74D$, which is slightly smaller than that at $\mathrm{Re}=230$ reported by Williamson (1992). This is probably due to the difference in Reynolds number. The streamwise vortices can be seen in the scale of $|\omega_x|=1$ after $Ut/D>65$ and become stronger and stronger with time. Although the streamwise vortices exist prior to $Ut/D=65$, they are too weak to be observed in the iso-surface plot of the scale $|\omega_x|=1$. In Fig. 4(b), the iso-surfaces of the spanwise vorticity components are still in the shape of continuous tubes. But they are uneven along the spanwise direction. In this instant, the turbulence in the vortex formation region is still rather weak. As the vortices are shed from the cylinder, they are distorted by the streamwise vortices. The vortex structures shown in Fig. 4 agree well with those observed previously at low Reynolds numbers (Williamson, 1992).

When turbulence intensifies, the shear layer instability happens under the effect of the uneven streamwise vorticity. The instability of the shear layer conversely enhances the turbulence. After $Ut/D=85$, the flow becomes fully three-dimensional. Bloor (1964) and Wei and Smith (1986) reported that the shear layer instability is the way of transition to turbulence at high Reynolds numbers (above 1000). Fig. 5(a) shows the iso-surfaces ($|\omega_x|=1$) of the streamwise vorticity for $\alpha=0^\circ$ at the moment $Ut/D=400$. The streamwise vorticity iso-surfaces are strongly irregular in the wake. Some of the iso-surfaces have similar shapes as those shown in Fig. 4(a), but they are in a very irregular alignment. It was found that the vortices were not shed from the cylinder surface at the same time, which was different from that shown in Fig. 4(a). They stretch in directions which deviate slightly from the streamwise direction. The interaction among them (combination, splitting or cancellation) leads to a chaos. Karniadakis and Triantafyllou (1992) also reported a chaotic state of the turbulent flow in the wake of a circular cylinder. Fig. 5(b) shows the iso-surfaces ($|\omega_z|=1$) of the spanwise vorticity. In the fully turbulent wake, the phase variation of the spanwise vortex shedding along the cylinder becomes very strong. From Fig. 5(b), it can be seen that the continuity of the tubular iso-surfaces of $\omega_z=-1$ breaks when the spanwise vortices are convected downstream, leading to the dislocation of the vortices. The spanwise vortices in Fig. 5(b) break down faster than that in Fig. 4(b).

When the flow approaches the cylinder at a yawed angle, the wake flow features are different. Fig. 6(a) shows the computed three-dimensional streamlines in the wake of the cylinder for $\alpha=45^\circ$. Fig. 6(c) reproduces the flow visualization of the streaklines by Kozakiewicz et al. (1995) for the same α. The streamlines that approach the leading edge of the cylinder bend to the cross cylinder direction after they slide some distance along the spanwise direction. After passing the cylinder, some of them are trapped into the principal spanwise vortex and move in the spanwise direction of the cylinder in helical tracks, while others move in the mean stream direction. The velocity at the centre of the principle vortex points to the cylinder's spanwise direction. Due to this flow pattern in the wake of a yawed cylinder, it is expected that, if there are particles in the fluid (such as suspended sediment or pollutant), the spanwise streamlines would make them drift along the cylinder spanwise direction for a certain distance. Once the principal spanwise vortex is shed from the cylinder surface, the streamlines that are trapped in it are released and their directions change back to the incoming flow direction. The present calculated streamlines in the wake agree well with the flow visualization by Kozakiewicz et al. (1995) (Fig. 6(c)) at the same yaw angle.

Fig. 7 shows the contours of the cross-axis vorticity magnitude $\omega_c=\sqrt{\omega_x^2+\omega_y^2}$, the spanwise vorticity ω_z, and the relative spanwise velocity $\tilde{w}=w/U_T$ for $\alpha=45^\circ$, where $U_T=U\sin\alpha$ is the incoming flow velocity component parallel to the cylinder. Both cross-axis vortices and the spanwise vortices reach their maximum values (in either negative or positive direction) at about the same positions (Fig. 7(a) and (b)). By comparing Fig. 7(b) and (c), it can be seen that the spanwise velocity reaches its minimum values where the cross-axis vorticity reaches its maximum. Moore (1956), Marshall (2003) and Thakur et al. (2004) also reported the phenomenon of deficit (spanwise velocity lower than the surrounding fluid, within the wake vortex cores) of the spanwise velocity within the vortex cores. Fig. 8 shows the distribution of the time averaged $\tilde{w}$ over the period of $150<Ut/D<400$ along the x-axis. It can be seen that the minimum mean $\tilde{w}$ occurs at about $x/D=1.25$ for all α. It decreases with the increase of α. The reduction of $\tilde{w}$ is the strongest when $\alpha=60^\circ$.

Fig. 9(a) shows the iso-surface of the spanwise vorticity $|\omega_z|=0.5$ for $\alpha=45^\circ$ at $Ut/D=400$. The spanwise vortices in the wake of the cylinder exhibit helical shapes. Experimental visualizations (Friehe and Schwarz, 1968; Ramberg, 1983) of flow past a yawed cylinder showed that the spanwise vortices in the wake of the cylinder were oriented at approximately the same angle as the cylinder for $\alpha<45^\circ$. The shedding angle of the spanwise vortex in Fig. 9(a) is well defined. Apparently, it is parallel to the cylinder axis. Fig. 9(b) is the iso-surface of the spanwise vorticity $|\omega_z|=0.25$ for $\alpha=60^\circ$. The vortex shedding angle is less well defined as compared with Fig. 9(a) even though the wake vortices are overall parallel to the cylinder. The shape of the vortices is twisted. Locally the spanwise vortices may or may not be parallel to the cylinder. Ramberg (1983) and Lucor and Karniadakis (2003) found that the spanwise wake vortices oriented at a smaller angle than the yaw angle of the cylinder if $\alpha>45^\circ$, which was slightly different from what was

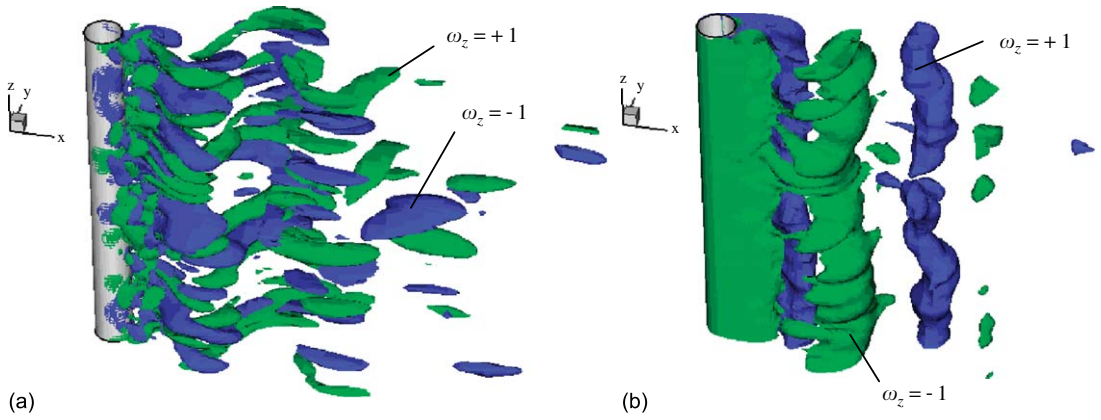

Fig. 5. Vorticity iso-surfaces for $\alpha = 0^\circ$ and $Ut/D = 400$: (a) $|\omega_x| = 1$ and (b) $|\omega_z| = 1$.

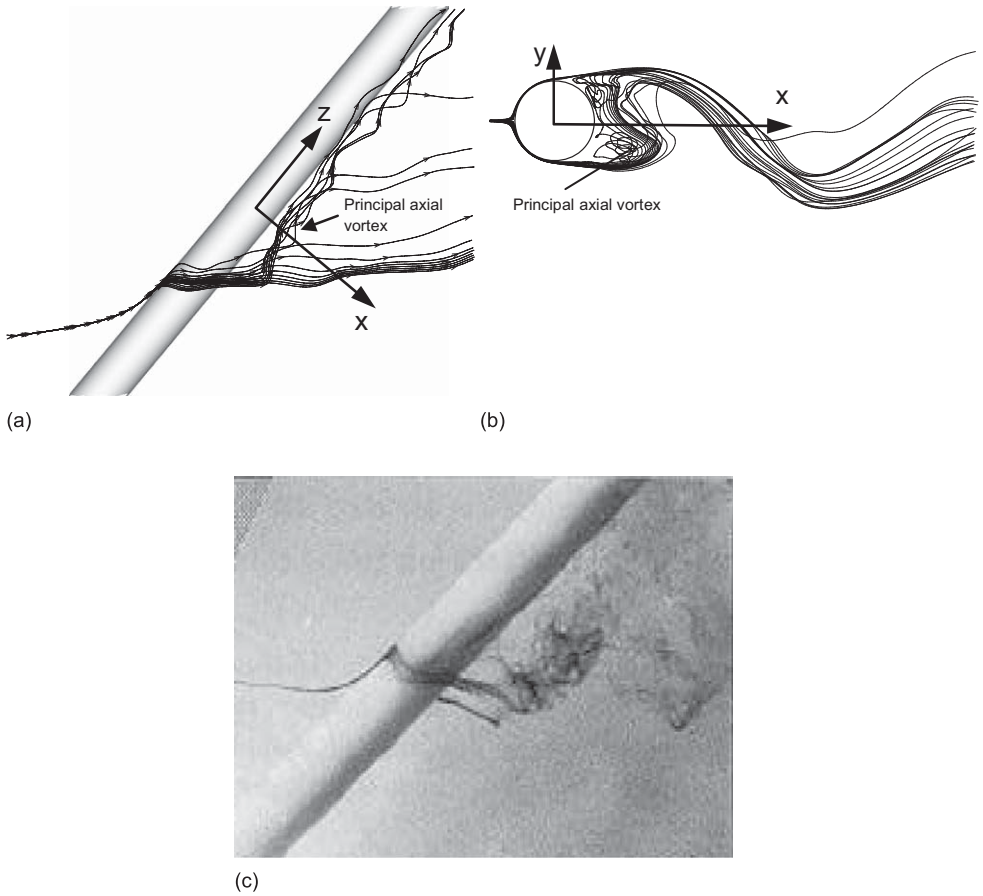

Fig. 6. Comparison of the wake flow for $\alpha = 45^\circ$: (a) side view of the streamlines, (b) top view of the streamlines and (c) flow visualization by Kozakiewicz et al. (1995) (Re = 1700).

observed in the present study. It was found that vortices right behind the cylinder propagate not only in the incoming flow direction, but also in the cylinder's spanwise direction. This is because of the spanwise streamlines as shown in Fig. 6(a). Vortices far away downstream the cylinder propagates mainly in the incoming flow direction.

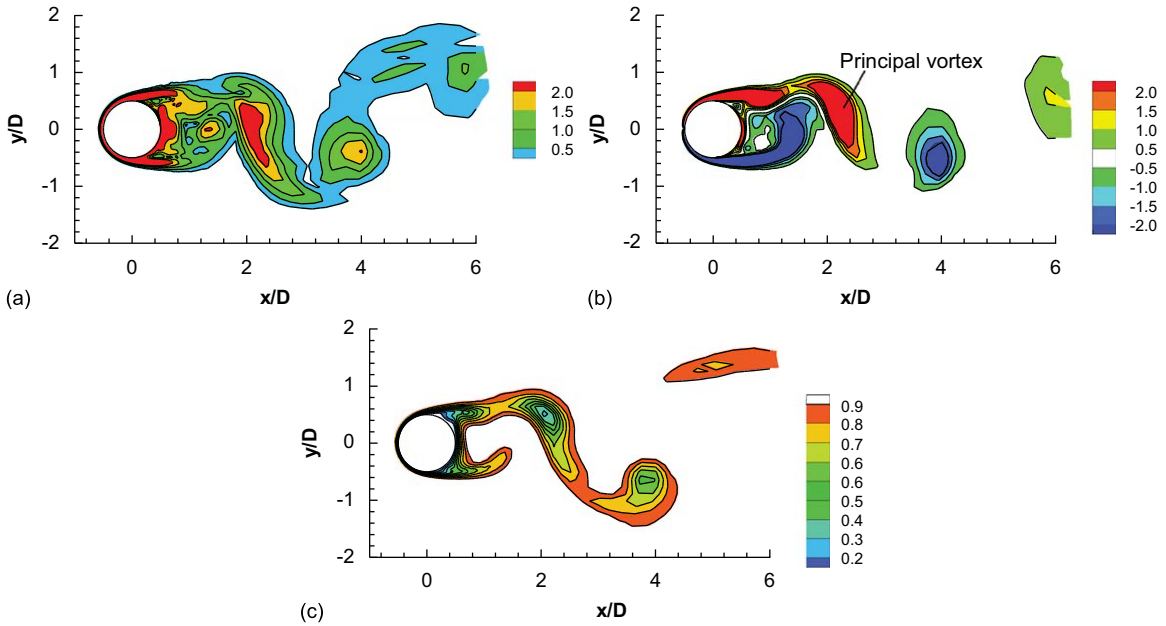

Fig. 7. Contours of cross-axis vorticity magnitude ω_c, spanwise vorticity ωz and axial velocity $\tilde{w}$ at section $z = 0$ and at the moment $Ut/D = 400$ for $\alpha = 45°$: (a) $\omega = \sqrt{\omega_x^2 + \omega_y^2}$, (b) ωz and (c) $\tilde{w} = w/U_T$.

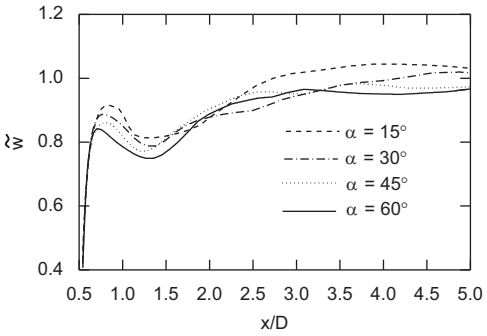

Fig. 8. Distributions of time-averaged mean axial velocity along x-axis.

Fig. 10 shows the mean streamlines in the x–y plane at $z = 0$ for various yaw angles. The mean streamlines are obtained by averaging the velocity over the time period between $Ut/D = 150$ and 450. Results for the case of $\alpha = 0°$ obtained using a two-dimensional numerical model (Zhao et al., 2007) are also included in Fig. 10(d). It is seen that the 3-D model results are significantly different from that of the 2-D model. The size of the recirculation zone from the 2-D simulation is about 50% smaller than those obtained using the 3-D model for $\alpha = 0°$. This difference between the 2-D and 3-D solutions were also found by Mittal and Balachandar (1995) and Lei et al. (2001). The length of the recirculation zone in the x-direction is about $1.5D$ for $\alpha = 0°$, which is close to the value of 1.35 reported by Honji and Taneda (1969). The shape and size of the recirculation zone in the wake of the cylinder for different α are almost the same. The difference between the length of the recirculation zone in the x-direction at $\alpha = 30°$ and that for $\alpha = 0°$ is about 12%, and that between $\alpha = 60°$ and 0° is about 9%.

Fig. 11 shows the time-averaged mean pressure distribution along the cylinder's circumference in the cross-cylinder plane at $z = 0$. The mean pressure is obtained by averaging the pressure over the time period from $Ut/D = 150$ to 450. The pressure coefficient in Fig. 11(a) is defined as $C_p = (p - p_s)/(\rho U^2/2)$, where p_s is the pressure at the position of $\theta = 0$. It can be seen that, with the increase of α, the pressure difference between the leading and trailing edges decreases. This makes the dimensional force in x-direction on the cylinder decrease with the decreasing α, if the incoming flow velocity

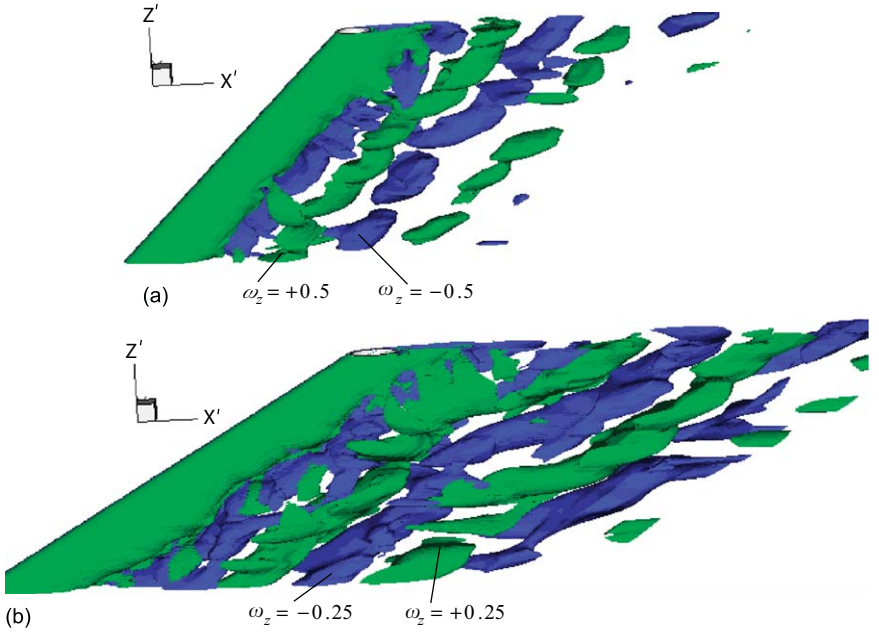

Fig. 9. Spanwise vorticity contours for yawed cylinder at $\alpha = 45^\circ$ and 60°: (a) $|\omega_z| = 0.5$ and $\alpha = 45^\circ$ and (b) $|\omega_z| = 0.25$ and $\alpha = 60^\circ$.

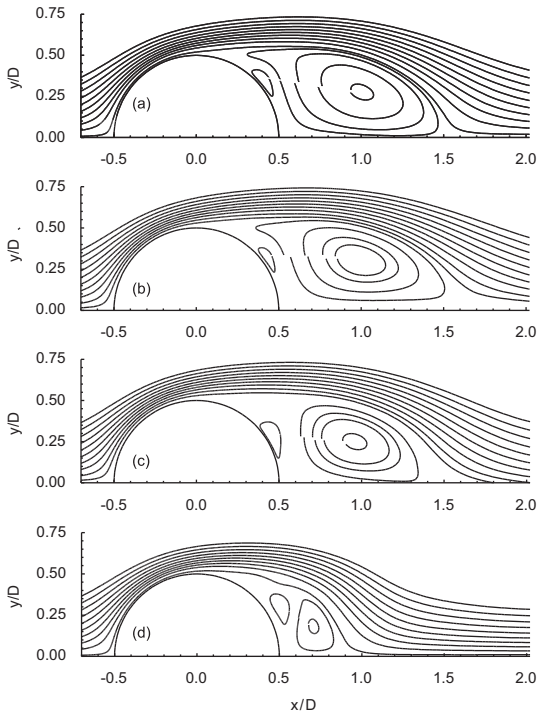

Fig. 10. Mean streamlines in the x–y plane: (a) $\alpha = 0^\circ$, (b) $\alpha = 30^\circ$, (c) $\alpha = 60^\circ$, and (d) $\alpha = 0^\circ$ by 2D model.

U is constant. The pressure coefficients C_{pn} in Fig. 11(b) are normalized by the velocity component U_n which is perpendicular to the cylinder, namely, $C_{pn} = (p - p_s)/(\rho U_n^2/2)$. It can be seen that there is little difference among the pressure coefficients for various yaw angles if they are normalized by U_n. This means that the independence principle

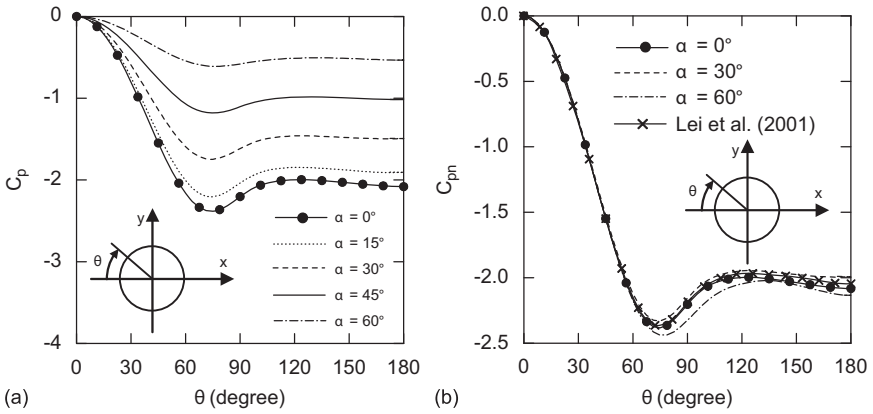

Fig 11. Time averaged pressure distributions along cylinder surface at section $z = 0$: (a) $C_p = (p-p_s)/(\rho DU^2/2)$ and (b) $C_{pn} = (p-p_s)/(\rho DU^2/2)$.

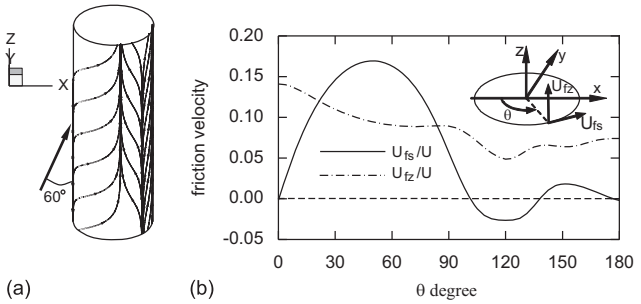

Fig. 12. Friction velocity distribution along the cylinder surface for $\alpha = 60^\circ$: (a) 3-D streamlines plotted according to the friction velocity and (b) friction velocity distribution along a circumference of the cylinder ($\alpha = 60^\circ$).

applies to the pressure along the cylinder surface. In Fig. 11(b), the results obtained by Lei et al. (2001) using the finite difference method (FDM) are also included. The two sets of numerical result for $\alpha = 0^\circ$ agree well with each other.

Fig. 12(a) shows the streamlines along the cylinder surface plotted according to the time-averaged friction velocity. The friction velocity vector $\vec{U}_f$ is defined by $\vec{U}_f = (\vec{\tau}/\rho)^{1/2}$, where $\vec{\tau}$ is the shear stress vector. Fig. 12(b) shows the distribution of the friction velocity components U_{fs} and U_{fz}, which are defined at the top-left corner of the figure, along a circumference of the cylinder at $z = 0$. The position angle θ is defined as the angle measured from the front edge of the cylinder. It can be seen that the friction velocity is in the spanwise direction of the cylinder at the front edge of the cylinder ($U_{fs} = 0$). It biases towards the cross-cylinder plane when it goes to the trailing edge of the cylinder. At about $\theta = 100^\circ$, which is the separation point of the shear layer, the direction of the friction velocity changes back to the positive z direction again. It can be seen in Fig. 12(b) that the friction velocity U_{fz} is always positive. This leads to a shear force on the cylinder surface in the z direction.

3.3. Strouhal number

Fig. 13 shows the time history of the force coefficients for $\alpha = 45^\circ$. The transition of the flow from 2-D to 3-D occurs after $Ut/D = 110$, which is delayed compared with that for $\alpha = 0^\circ$ (Fig. 3). It is found that the increase of α delays the transition in the numerical simulation. The flow becomes fully three-dimensional after $Ut/D = 150$ for the maximum calculated α ($= 60^\circ$). A FFT analysis is applied to the time series of the fluctuating lift coefficients over the period of $150 < Ut/D < 450$. Fig. 14 shows the power spectra of the sectional lift coefficients at the cross section $z = 0$. It can be seen that all spectra have a pronounced sharp peak, indicating apparent vortex shedding at these frequencies. For $\alpha = 0^\circ$, the peak occurs at $fD/U_n = 0.210$, which agrees well with previous results in cross-flows. With the increase of the yaw angle, the peak locations do not change apparently. Moreover, the peak region for $\alpha = 60^\circ$ is broader than that for

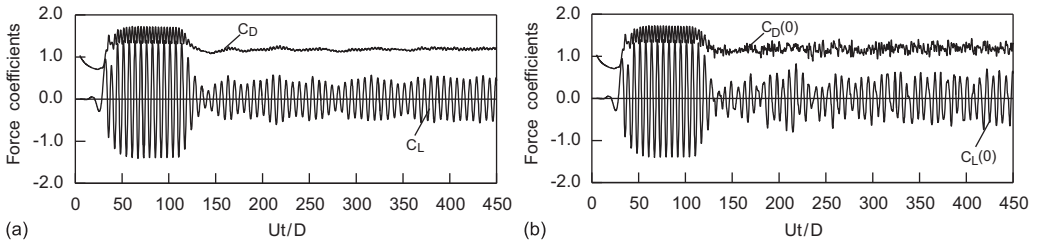

Fig. 13. Time history of force coefficients for $\alpha = 45^\circ$: (a) total and (b) sectional ($z_0 = 0$).

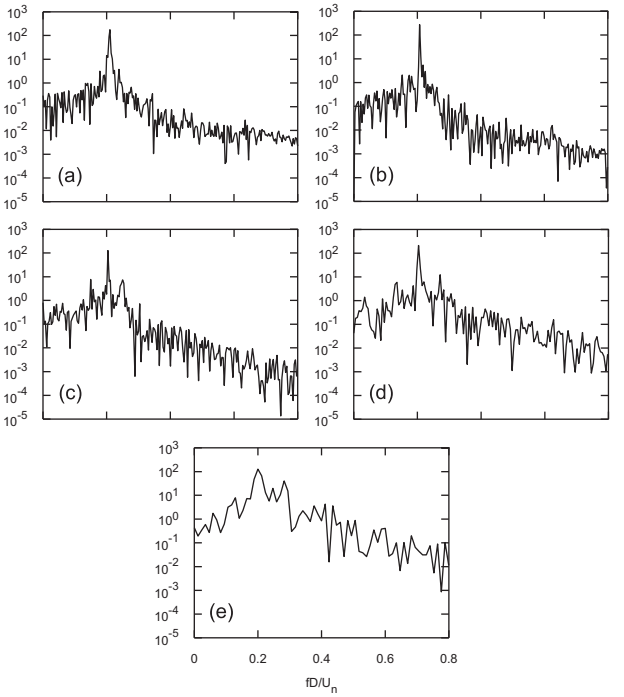

Fig. 14. Spectra of the fluctuating lift coefficient: (a) $\alpha = 0^\circ$, (b) $\alpha = 15^\circ$, (c) $\alpha = 30^\circ$, (d) $\alpha = 45^\circ$ and (a) $\alpha = 60^\circ$.

$\alpha = 0^\circ$. This indicates that with the increase of the yaw angle, the rate of the breakdown of the vortex structures is increased. Fig. 15 shows the comparison of the computed Strouhal number with the experimental data by Ramberg (1983) and the fitted curve from experimental data by Van Atta (1968). The Strouhal number is defined as the peak frequencies shown in Fig. 14 and the velocity component normal to the cylinder. In Fig. 15, St_0 represents the Strouhal number for $\alpha = 0^\circ$. The results by Ramberg (1983) are those for flow past a cylinder of $90D$ long. The three sets of data agree with each other very well when $\alpha \leqslant 30^\circ$ and all of them follow the cosine law. The discrepancy happens when $\alpha = 30^\circ$and it increases with the increase of α. The computed Storuhal number at $\alpha = 60^\circ$ is 20% smaller than the measured values by Ramberg (1983). There is also large difference between the experimental data by Ramberg (1983) and that by Van Atta (1968) when $\alpha = 60^\circ$. The discrepancies among these data may be attributed to the following reasons, among many factors. Firstly, the length of the cylinder used in the experiment is different from that used in the numerical modelling. In the present study, a periodic boundary condition at the two ends was employed to simulate an infinite long cylinder. This implies that the flow can come into or out of the computational domain through the top and bottom boundaries as shown in Fig. 1. In the experiment of Ramberg (1983) the top and the bottom boundaries are glass walls which are wind-tight. Secondly, the Reynolds number for Van Atta's curve is in the transitional regime, whereas that in the present study and that of Ramberg are in the turbulent regime.

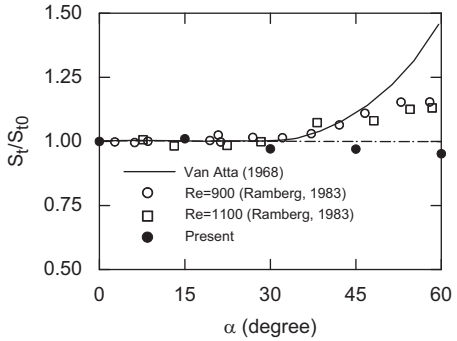

Fig. 15. Variation of Strouhal number with α.

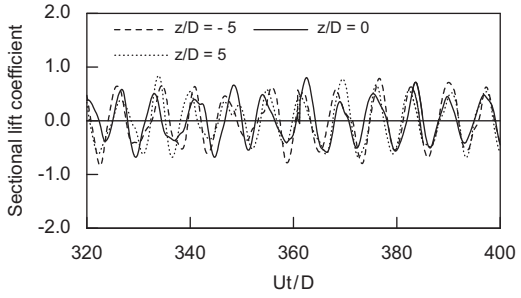

Fig. 16. Time history of the sectional lift coefficient at three sections for $\alpha = 45^\circ$.

3.4. Force coefficients

The variation of the wake flow in the cylinder's spanwise direction (as discussed above) makes the sectional lift force coefficient on a unit length of the cylinder vary along the cylinder. Fig. 16 shows the time history of the sectional lift coefficient for $\alpha = 45^\circ$ at three sections. The total and sectional force coefficients are calculated by Eqs. (3) and (4), respectively. It is seen that the amplitudes and the frequencies of the lift force fluctuation at these three sections are basically the same. However, there is phase difference among them. This phenomenon indicates that there are phase differences among vortex shedding at different cross sections. If the force is averaged over time, no difference is found in terms of mean force at different cross-sections.

Fig. 17 shows the statistic values of the force coefficients, which were obtained according to the force time series between $Ut/D = 150$ and 450. The sectional force coefficients are measured at the cross section of $z = 0$. The total and sectional mean (time-averaged) drag coefficients in Fig. 17(a) are almost the same. The mean drag coefficient $\bar{C}_D$ changes little when α increases from 0° to 30°. It increases slightly with the increase of α when $\alpha > 30^\circ$ and reaches its maximum value of $\bar{C}_D = 1.27$ at $\alpha = 60^\circ$, which is 8% larger than the right attack angle case ($\alpha = 0^\circ$). There is apparent difference between the r.m.s. sectional drag coefficient and the r.m.s. total drag coefficient (Fig. 17(b)); the former is about twice of the latter when α is between 0° and 30°. When $\alpha > 30^\circ$, the r.m.s. sectional drag coefficient increases with the increase of α, whereas the r.m.s. total drag coefficient decreases. The r.m.s. sectional lift coefficient is around 7–10% larger than the r.m.s. total lift coefficient in the calculated range of α (Fig. 17(c)). The difference between the total and the sectional r.m.s. force coefficients is mainly because of the phase variation of the vortex shedding along the cylinder's spanwise direction. The r.m.s. lift coefficient decreases slightly with the increase of α when $\alpha \leqslant 30^\circ$ and reaches its minimum value at $\alpha = 30^\circ$. The r.m.s. lift coefficient at $\alpha = 30^\circ$ is about 25% smaller than that of $\alpha = 0^\circ$. It increases with α when $\alpha > 30^\circ$. The r.m.s. lift coefficient at $\alpha = 60^\circ$is 20% larger than that at $\alpha = 0^\circ$. The 2-D numerical results overestimate the mean drag coefficient, r.m.s. drag coefficient and especially the r.m.s. lift coefficient because the 2-D model omits the variation of the flow in the cylinder's spanwise direction. This is equivalent to that the vortex shedding is synchronized in the spanwise direction. The overestimation of force coefficients by the 2-D models had been reported by Zhao et al. (2005) and Lei et al. (2000).

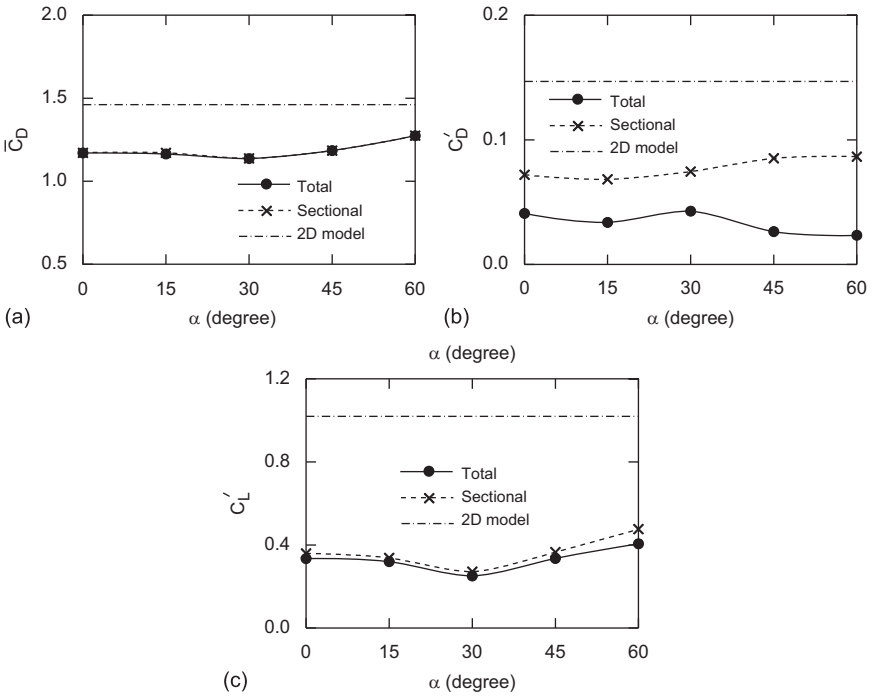

Fig. 17. Time-averaged and root-mean-square (r.m.s.) force coefficients at various yaw angles: (a) mean drag, (b) r.m.s drag coefficient and (c) r.m.s. lift coefficient.

4. Conclusions

Flow past a circular cylinder at yaw angles in the range of 0–60° was investigated numerically by solving the three-dimensional Navier–Stokes equations directly using a finite element method. The results were compared with the flow visualization in the experiments. The effects of the yaw angle on vortex structures and the force coefficients were examined. The results are summarized as follows:

(1) In the numerical simulation the flow in the early stage of the transition period from 2-D to 3-D is similar to the flow when Reynolds number is in the transitional regime. The streamwise vortices occur at the beginning of the transition. The pattern of the streamwise vortices changes from regular to irregular. The streamwise vortices become stronger with time and affect the shear layer at the late stage of the transition period. The vortex dislocation happens at the end of the transition period.

(2) Near the centre of the principal spanwise vortex, the streamlines are in the spanwise direction of the cylinder and in a helical shape. The velocity at the centre of the principal vortex points to the cylinder's spanwise direction. This makes the velocity in the vortex right behind the cylinder to have a strong spanwise component. When vortices are far downstream of the cylinder, they are convected in the incoming flow direction.

(3) The computed spanwise vortices are parallel to the cylinder for all α. This leads to the Strouhal number closely following the cosine law. The numerical results of Strouhal numbers agree well with the experimental data when $\alpha \leqslant 30^\circ$ and are slightly smaller than experimental data when $\alpha > 30^\circ$. The maximum discrepancy ($\approx 20\%$) between the computed Strouhal number and the measured values happens at $\alpha = 60^\circ$.

(4) The r.m.s. sectional force coefficients, which are computed by integrating the pressure and shear stress around the circumference of a cross-section of the cylinder surface, are different from the r.m.s. total force coefficients calculated by integrating over the whole cylinder surface. The r.m.s. sectional drag coefficient is about twice of the r.m.s. total drag coefficient. The r.m.s. sectional lift coefficient is also 7–10% larger than the r.m.s. total lift coefficient. However, the mean sectional drag coefficient is the same as the mean total drag coefficient.

(5) The independence principle applies very well to the mean drag coefficient when α is in the range of 0–30°. The maximum mean drag coefficient happens when $\alpha = 60^\circ$, and is about 10% larger than that at $\alpha = 0^\circ$. The r.m.s. lift

coefficient reaches its minimum value at $\alpha = 30^\circ$, which is 25% smaller than that when $\alpha = 0^\circ$. The r.m.s. lift coefficient for $\alpha = 60^\circ$ is 20% larger than the right attack angle case.

Acknowledgement

The authors would like to acknowledge the supports from Australia Research Council through ARC Discovery Projects Program Grant no. DP0557060 and CSIRO Flagship Collaboration Cluster on Subsea Pipelines.

Appendix. Petrov–Galerkin finite element formulation

The computational domain was divided into hexahedron eight-node tri-linear elements. Fig. 2 is an example of the meshes for $\alpha = 45^\circ$. One-third of the elements are not shown in Fig. 2 in order to see the mesh distribution along the span direction of the cylinder. The pressure and the velocity in the computational domain are interpolated by the shape function by $f = \sum N_k f_k$, where f represents velocity or pressure, f_k is the value of f at kth node and N_k is the shape function. The weighted residual formula for Eq. (1) is expressed as

$$\int_{\Omega} (Wu_{i,t} + Wu_j u_{i,j} + \frac{1}{\mathrm{Re}} W_{,j} u_{i,j} + Wp_{,i})\,\mathrm{d}\Omega - \int_{\Gamma} Wu_{i,n}\,\mathrm{d}\Gamma = 0, \tag{A1}$$

where W *is* the weighting function, Ω represents the computational domain, Γ represents the boundary of the domain, $u_{i,n}$ is the gradient of u_i in the normal direction of the boundaries outwards. When performing the integration numerically within an element, a hexahedron eight-node finite element is transformed into a cubic element with a boundary length of 2 as shown in Fig. 18. The weighted residual formulation (A1) in the transformed coordinate $\xi_1\xi_2\xi_3$ system is expressed as

$$\int_{\bar{\Omega}} (Wu_{i,t} + WU_a u_{i/a} + \varepsilon_{ab} W_{/a} u_{i/b} + W\xi_{a,i} p_{/a}) J\,\mathrm{d}\bar{\Omega} - \int_{\bar{\Gamma}} Wu_{i,n} I\,\mathrm{d}\bar{\Gamma} = 0, \tag{A2}$$

where $\mathrm{d}\Omega = J\,\mathrm{d}\bar{\Omega}$, $\mathrm{d}\Gamma = I\,\mathrm{d}\bar{\Gamma}$, J and I denote the transformation Jacobians for domains and boundaries between the physical domain and the transformed domain, subscript "$/a$" represents the derivative with respect to ξ_a ($a = 1$, 2 and 3), $U_a = u_j \xi_{a,j}$ and $\varepsilon_{ab} = (1/\mathrm{Re})\xi_{a,j}\xi_{b,j}$.

The conventional Galerkin finite element method uses the shape function as the weighting function. The spurious node-to-node oscillations or wiggles occur if the solution is performed by a simple Galerkin finite element method. These wiggles often corrupt the solutions. The Petrov–Galerkin scheme is employed in this numerical model for eliminating the wiggles. In the Petrov–Galerkin formulation the standard Galerkin weighting functions are modified by adding a streamline upwind perturbation, which acts only in the flow direction (Brooks and Hughes, 1982; Kondo, 1994; Jester and Kallinderis, 2003). The weighting function for the Galerkin finite element method is the shape function, which is expressed as

$$W = N_1 N_2 N_3, \tag{A3}$$

where N_a is the one-dimensional shape function in the ξ_a direction. In the Petrov–Galerkin method the weighting function is modified as $w + \tilde{w}$, where $\tilde{w}$ is a perturbation function. By introducing the perturbation function, the element

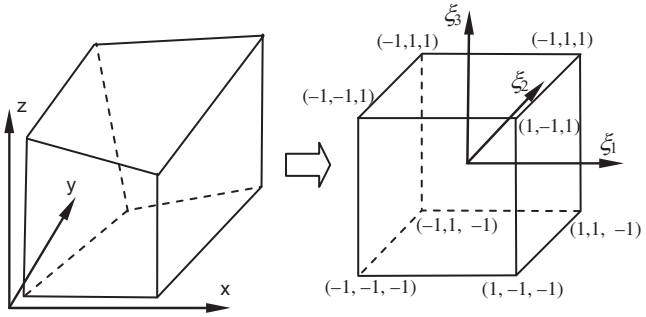

Fig. 18. Coordinate transformation for a finite element.

upwind of a node has a heavier weight than that downstream of a node. If the problem is one-dimensional, the perturbation term is defined by (Brooks and Hughes, 1982)

$$\tilde{W}_1 = \gamma U_1 \tilde{\xi}_1 \Delta_1 N_{1/1}, \tag{A4}$$

where the subscript 1 stands for one-dimensional, Δ_1 is the element size in the transformed domain, the artificial diffusion coefficient $\tilde{\xi}_1$ is defined as $\xi_1 = \coth(\psi) - 1/\psi$, where $\psi = U_1\Delta_1/2\varepsilon_{11}$ and γ is a constant. Raymond and Garder (1976) demonstrated that the phase errors are minimized if the constant $\gamma = 1/\sqrt{15}$ is employed for the transient case. In the three-dimensional case, the Petrov–Galerkin weighting function is expressed as

$$(N_1 + \tilde{W}_1)(N_2 + \tilde{W}_2)(N_3 + \tilde{W}_3). \tag{A5}$$

In this finite element model, only first order of $\tilde{W}_a$ is considered in the weighting function. So, the perturbation function used in this model is

$$\tilde{W} = (\tilde{W}_1 N_2 N_3 + N_1 \tilde{W}_2 N_3 + N_1 N_2 \tilde{W}_3), \tag{A6}$$

where $\tilde{W}_a$ ($a = 1$, 2 and 3) is obtained by Eq. (A4). The formation of the weighting perturbation function Eq. (A6) is determined in the transformed domain rather than in the physical domain. If an element's aspect ratio is about unity, it does not make much difference from that proposed by Brooks and Hughes (1982). In the boundary layer next to the wall, however, the size of the elements in the normal direction to the wall is much smaller (sometimes less than one-tenth) than that in the tangential direction in order to model the high velocity gradient. In the perturbation function by Brooks and Hughes the maximum element length among three dimensions is used as the representative element length when calculating the artificial diffusive factor. If an element's aspect ratio is high and the flow is not parallel to the element's length direction, this may lead to significant numerical diffusion. Excessive numerical diffusion in the cross-flow direction can be avoided by using Eq. (A6) in elements of high aspect ratio, because different artificial diffusive factors can be used in the three directions of the transformed domain.

After introducing the perturbation weighting function, the Petrov–Galerkin finite element formula Eq. (A2) is rewritten as

$$\int_{\bar{\Omega}} ((W + \tilde{W})u_{i,t} + (W + \tilde{W})U_a u_{i/a} + \varepsilon_{ab}(W + \tilde{W})_{/a} u_{i/b} + (W + \tilde{W})\xi_{a,i} p_{/a}) J \,\mathrm{d}\bar{\Omega} - \int_{\bar{\Gamma}} (W + \tilde{W}) u_{i,n} I \,\mathrm{d}\bar{\Gamma} = 0. \tag{A7}$$

A fractional step method is employed in the time integration of Eq. (A7). The velocity field satisfies the continuity equation exactly by using the fractional step method. It had been demonstrated that the fractional step method can be successfully applied to the finite element analysis (Donea et al., 1982; Ramaswamy and Jue, 1992; Ramaswamy, 1988). In the fractional step method, for a time interval from time $n\,\Delta t$ to $(n+1)\,\Delta t$, an intermediate velocity is firstly calculated by time-integrating FEM formula of a momentum equation in which the pressure term is omitted. The intermediate velocity does not necessarily satisfy the incompressibility condition. The final velocity at time $(n+1)\,\Delta t$ is calculated by solving a momentum equation with only the pressure, which is computed by solving a pressure Poisson equation. The details of the steps for solving Eq. (A7) are described as follows:

(a) A intermediate velocity $\hat{u}_i^{n+1}$ is firstly calculated by omitting pressure term in Eq. (A7). In this step, the convective term is considered explicitly and the diffusive term implicitly. The equation for $\hat{u}_i^{n+1}$ is

$$\int_{\bar{\Omega}} ((W + \tilde{W})\frac{1}{\Delta t}(\hat{u}_i^{n+1} - u_i^n) + (W + \tilde{W})U_a^n u_{i/a}^n + \varepsilon_{ab}(W + \tilde{W})_{/a} \hat{u}_{i/b}^{n+1}) J \,\mathrm{d}\bar{\Omega} - \int_{\bar{\Gamma}} (W + \tilde{W}) \hat{u}_{i,n}^{n+1} I \,\mathrm{d}\bar{\Gamma} = 0, \tag{A8}$$

where Δt is the computational time step, the subscript n represents the values at the time level $n\,\Delta t$.

(b) A pressure Poisson equation is solved for the pressure

$$p_{,jj}^{n+1} = \frac{1}{\Delta t} \hat{u}_{i,i}^{n+1}. \tag{A9}$$

This pressure Poisson equation is obtained by combining the continuity equation Eq. (2) and the Eq. (A11). The finite element formula for Eq. (A9) is

$$-\int_{\bar{\Omega}} W_{,j} p_j J \,\mathrm{d}\bar{\Omega} + \int_{\bar{\Gamma}} W p_{,n} I \,\mathrm{d}\bar{\Gamma} = \int_{\bar{\Omega}} W \frac{1}{\Delta t} \hat{u}_{i,i}^{n+1} J \,\mathrm{d}\bar{\Omega}. \tag{A10}$$

(c) The final velocity is calculated by including the pressure

$$\int_{\tilde{\Omega}} \left[\frac{1}{\Delta t} W(u_i^{n+1} - \hat{u}_i^{n+1}) + W \xi_{a,i} p_{/a} \right] J \, \mathrm{d}\tilde{\Omega} = 0. \tag{A11}$$

Because the upwind scheme is only for dealing with the instability due to the convective term, the perturbation term $\tilde{W}$ is only applied to Eq. (A8). Conventional Galerkin formulas were used to discretize Eq. (A10) and (A11).

References

Bloor, M.S., 1964. The transition to turbulence in the wake of a circular cylinder. Journal of Fluid Mechanics 19, 290–309.

Braza, M., Chassaing, P., Minh, H.H., 1986. Numerical study and physical analysis of the pressure and velocity fields in the near wake of a circular cylinder. Journal of Fluid Mechanics 165, 79–130.

Brooks, A.N., Hughes, T.J.R., 1982. Streaming upwind/Petrov–Galerkin formulations for convection dominated flow with particular emphasis on the incompressible Navier–Stokes equations. Computer Methods in Applied Mechanics and Engineering 32, 199–259.

Chiba, K., Horikawa, A., 1987. Numerical solution for the flow of viscoelastic fluids around an inclined circular cylinder. II. The hydrodynamic force on a circular cylinder. Rheologica Acta 26, 255–265.

Donea, J., Giuliani, S., Laval, H., Quartapelle, L., 1982. Finite element solution of the unsteady Navier–Stokes equations by a fractional step method. Computer Methods in Applied Mechanics and Engineering 30, 53–73.

Friehe, C.A., Schwarz, W.H., 1968. Deviations from cosine law for yawed cylindrical anemometer sensors. Journal of Applied Mechanics 35, 655–662.

Honji, H., Taneda, S., 1969. Unsteady flow past a circular cylinder. Journal of the Physical Society of Japan 27, 1668–1677.

Jester, W., Kallinderis, Y., 2003. Numerical study of incompressible flow about fixed cylinder pairs. Journal of Fluids and Structures 17, 561–577.

Kang, S., 2006. Uniform-shear flow over a circular cylinder at low Reynolds numbers. Journal of Fluids and Structures 22, 541–555.

Karniadakis, G.E., Triantafyllou, G.S., 1992. Three-dimensional dynamics and transition to turbulence in the wake of bluff objects. Journal of Fluid Mechanics 238, 1–30.

King, R., 1977. Vortex excited oscillations of yawed circular cylinders. ASME Journal of Fluids Engineering 99, 495–502.

Kondo, N., 1994. Third-order upwind finite element solutions of high Reynolds number flows. Computer Methods in Applied Mechanics and Engineering 112, 227–251.

Kozakiewicz, A., Fredsøe, J., Sumer, B.M., 1995. Forces on pipelines in oblique attack: steady current and waves. In: Proceedings of the 5th International Offshore and Polar Engineering Conference, The Hague, The Netherlands, vol. 2, pp. 174–183.

Lei, C., Cheng, L., Kavanagh, K., 2000. A finite difference solution of the shear flow over a circular cylinder. Ocean Engineering 27, 271–290.

Lei, C., Cheng, L., Kavanagh, K., 2001. Spanwise length effects on three-dimensional modelling of flow over a circular cylinder. Computer Methods in Applied Mechanics and Engineering 190, 2909–2923.

Lucor, D., Karniadakis, G.E.M., 2003. Effects of oblique inflow in vortex-induced vibrations. Flow, Turbulence and Combustion 71, 375–389.

Marshall, J.S., 2003. Wake dynamics of a yawed cylinder. ASME Journal of Fluids Engineering 125, 97–103.

Mittal, R., Balachandar, S., 1995. Effect of three-dimensionality on the lift and drag of nominally two-dimensional cylinders. Physics of Fluids 7, 1841–1865.

Moore, F.K., 1956. Yawed infinite cylinders and related problems—independence principle solutions. Advances in Applied Mechanics 4, 180–187.

Niemann, H.J., Hölscher, N., 1990. A review of recent experiments on the flow past circular cylinders. Journal of Wind Engineering and Industrial Aerodynamics 33, 197–209.

Norberg, C., 2001. Flow around a circular cylinder: aspects of fluctuating lift. Journal of Fluids and Structures 15, 459–469.

Ramaswamy, B., 1988. Finite element solution for advection and natural convection flow. Computers and Fluids 16, 349–388.

Ramaswamy, B., Jue, T.C., 1992. Some recent trends and developments in finite element analysis for incompressible thermal flow. International Journal for Numerical Methods in Engineering 35, 671–707.

Ramberg, S., 1983. The effects of yaw and finite length upon the vortex wakes of stationary and vibrating circular cylinders. Journal of Fluid Mechanics 128, 81–107.

Raymond, W.H., Garder, A., 1976. Selective damping in a Galerkin method for solving wave problems with variable grids. Monthly Weather Review 104, 1583–1590.

Roshko, A., 1954. On the development of turbulent wakes from vortex streets. NACA Report 1191, 1–23.

Schewe, G., 1983. On the force fluctuations acting on a circular cylinder in cross-flow from subcritical up to transcritical Reynolds numbers. Journal of Fluid Mechanics 133, 265–285.

Thakur, A., Liu, X., Marshall, J.S., 2004. Wake flow of single and multiple yawed cylinders. ASME Journal of Fluids Engineering 126, 861–870.

Tsutsui, T., Igarashi, T., Kamemoto, K., 1997. Interactive flow around two circular cylinders of different diameters at close proximity. Experiment and numerical analysis by vortex method. Journal of Wind Engineering and Industrial Aerodynamics 69–71, 279–291.

Van Atta, C.W., 1968. Experiment on vortex shedding from yawed circular cylinders. AIAA Journal 6, 931–933.
Wei, T., Smith, C.R., 1986. Secondary vortices in the wake of circular cylinders. Journal of Fluid Mechanics 169, 513–533.
Williamson, C.H.K., 1988. The existence of 2 stages in the transition to three-dimensionality of a cylinder wake. Physics of Fluids 31, 3165–3168.
Williamson, C.H.K., 1991. The formation of spot-like Λ-structures caused by vortex dislocations in a wake. In: Proceedings of the 8th Symposium on Turbulent Shear Flows, Munich, Germany.
Williamson, C.H.K., 1992. The Natural and forced formation of spot-like 'vortex dislocations' in the transition of a wake. Journal of Fluid Mechanics 243, 393–441.
Zhang, J., Dalton, C., 1998. A three-dimensional simulation of a steady approach flow past a circular cylinder at low Reynolds number. International Journal for Numerical Methods in Fluids 26, 1003–1022.
Zhao, M., Cheng, L., Teng, B., Liang, D., 2005. Numerical simulation of viscous flow past two circular cylinders of different diameters. Applied Ocean Research 27, 39–55.
Zhao, M., Cheng, L., Teng, B., Dong, G., 2007. Hydrodynamic forces on dual cylinders of different diameters in steady currents. Journal of Fluids and Structures 23, 59–83.